International Journal of Minerals, Metallurgy and Materials
Volume 25, Number 6, June 2018, Page 623
https://doi.org/10.1007/s12613-018-1609-4

Effect of main inclusions on crack initiation in bearing steel in the very high cycle fatigue regime

Chao Gu[1)], *Yan-ping Bao*[1)], *Peng Gan*[1)], *Min Wang*[1)], *and Jin-shan He*[2)]

1) State Key Laboratory of Advanced Metallurgy, University of Science and Technology Beijing, Beijing 100083, China
2) Steel Institute, RWTH Aachen University, Aachen 52072, Germany
(Received: 6 September 2017; revised: 4 December 2017; accepted: 27 December 2017)

Abstract: This work aims to investigate the effect of main inclusions on crack initiation in bearing steel in the very high cycle fatigue (VHCF) regime. The size and type of inclusions in the steel were quantitatively analyzed, and VHCF tests were performed. Some fatigue cracks were found to be initiated in the gaps between inclusions (Al_2O_3, MgO-Al_2O_3) and the matrix, while other cracks originated from the interior of inclusions (TiN, MnS). To explain the related mechanism, the tessellated stresses between inclusions and the matrix were calculated and compared with the yield stress of the matrix. Results revealed that the inclusions could be classified into two types under VHCF; of these two, only one type could be regarded as holes. Findings in this research provide a better understanding of how inclusions affect the high cycle fatigue properties of bearing steel.

Keywords: very high cycle fatigue; bearing steel; inclusions; tessellated stress; crack initiation

1. Introduction

With the development of metallurgical technology and the industry, the fatigue property of many materials has considerably improved. A large amount of research has focused on very high cycle fatigue (VHCF), where inclusions play an important role in failure. According to previous work [1–4], a circular area called "fish-eye" could be observed when crack initiation is caused by internal inclusions. Wang *et al.* [5] claimed that most of the fatigue life of a material is spent in the formation of round structures, which are caused by a rough area inside the "fish-eye." This area has been given different names when observed by different apparatuses: "optically dark area (ODA)" by Murakami *et al.* [6–8], "granular bright facets" by Shiozawa *et al.* [9–10], and "fine granular area (FGA)" by Sakai *et al.* [11]. In this paper, the term ODA is adopted.

Considering the effect of inclusions on fatigue failure, these inclusions are often assumed to be holes by many researchers. Based on this assumption, Murakami *et al*. [12–14] proposed an "equivalent projected area model" and estimated the critical size of inclusions to determine the high cycle fatigue of high-strength steel. Sun *et al*. [15] developed another model to the estimate fatigue lifetime and speed of failure with ODA fractures by observing cumulative fatigue damage in several samples. Li *et al*. [16] proposed a statistical method to estimate the distribution characteristics of high carbon chromium-bearing steel based on the Weibull distribution and parameter optimization.

Several researchers have recently proposed that various types of inclusions could exert different influences on fatigue life [17–18]. Spriestersbach *et al*. [17] determined the threshold values of stress intensity for crack initiation by FGA formation in the VHCF regime by runout tests and claimed that the VHCF behavior is highly dependent on the types of inclusions in the material. Karr *et al*. [18] also studied the VHCF life properties of 18Ni maraging steel with different kinds of inclusions. Despite the importance of the topic, however, limited research has focused on the effects of inclusion types on VHCF from the viewpoint of tessellated stress between inclusions and a matrix caused by variations in temperature during heat treatment.

Corresponding author: Yan-ping Bao E-mail: baoyp@ustb.edu.cn

In this paper, the effect of main inclusions on crack initiation in bearing steel in the VHCF regime was presented based on calculations of tessellated stresses between these inclusions and the steel matrix. The VHCF properties of Al-deoxidized bearing steel were also tested by an ultrasonic fatigue testing machine. The nanoindentation test and the inclusion automatically analysis method were applied to characterize the steel matrix and inclusion distribution. The present research provides a theoretical foundation for further quantitative research on the influences of different types of inclusions on the VHCF life of bearing steel.

2. Experimental

2.1. Materials and specimens

The material used in this study was the high carbon–chromium-bearing steel GCr15. The chemical composition of the investigated steel is shown in Table 1. The main deoxidant used in the smelting of this steel was Al, and the steel was prepared as round bars with a diameter of 35 mm after hot rolling. Heat treatment procedures consisted of annealing, quenching, and tempering. The quenching condition was vacuum oil quenching after holding for 20 min at 835°C. The tempering condition was holding for 120 min at 180°C. The microstructure of the steel was identified as martensite, as shown in Fig. 1.

Table 1. Chemical composition of GCr15 bearing steel wt%

C	Cr	Si	Mn	P	S	Cu	Al
1.03	1.37	0.21	0.33	0.0110	0.0008	0.0744	0.0110

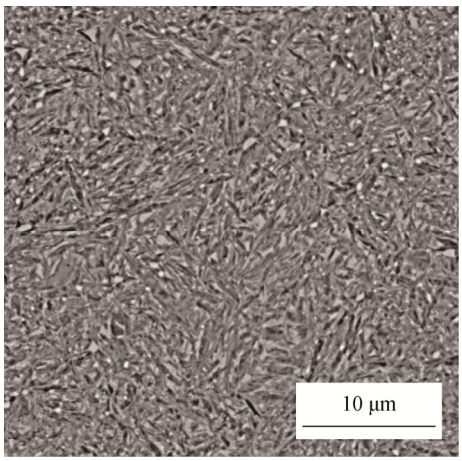

Fig. 1. Microstructure of GCr15 bearing steel.

The specimens in the present work were taken from the edges of the bars along the axial direction to obtain even microstructure and inclusion conditions. The specimen geometry for the fatigue tests is shown in Fig. 2. The middle portion of each specimen was polished along the circumferential direction to reduce the influence of surface roughness on its fatigue properties.

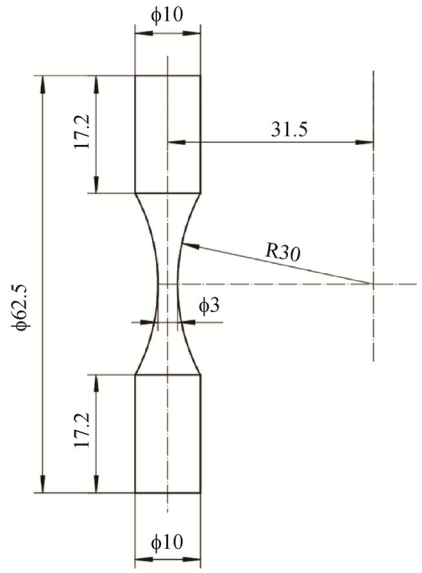

Fig. 2. Geometry of the specimens used for the fatigue tests (unit: mm).

2.2. Fatigue testing

Twelve specimens were subjected to fatigue tests under a resonance frequency of 20 kHz, and the loading condition was fully reversed tension–compression ($R = -1$). To ensure that the material was not affected by temperature, the tests were performed in air-cooled conditions. The temperature was kept below 50°C during the tests, and the stress amplitude was set to around 1000–1300 MPa. The ultrasonic fatigue testing machine applied in the present work is shown in Fig. 3. After the specimens had broken, their fracture surfaces were observed by scanning electron microscopy (SEM). The chemical composition of the material at the point of crack initiation was also analyzed by energy disperse spectroscopy (EDS).

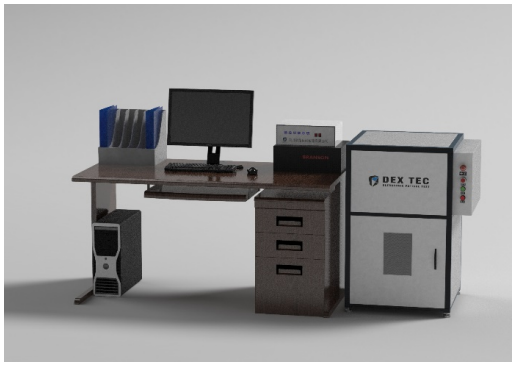

Fig. 3. Ultrasonic fatigue testing machine used in this work.

2.3. Inclusion and nanoindentation analyses

Inclusions measuring over 1 μm around the center of the specimens used for fatigue tests were automatically scanned; the scan area was 38.2 mm^2. Nanoindentation tests were performed on the steel matrix by a triangular-pyramid-diamond indenter (Nano Indenter XP). The corresponding load versus displacement curves were then measured and compared with those of the inclusions. Here, the displacement and load resolutions were less than 0.01 nm and 50 nN, respectively.

3. Results and discussion

3.1. Main inclusions in bearing steel

After scanning by the automatic inclusion analyzing technology, the main inclusions in Al-deoxidized bearing steel GCr15 were identified as Al_2O_3, MgO-Al_2O_3, MnS, and TiN. Figs. 4(a) and 4(b) respectively show the size distribution and number density of these inclusions. The average sizes of Al_2O_3, MgO-Al_2O_3, MnS, and TiN were 2.0, 2.1, 3.0, and 1.8 μm, respectively. Al_2O_3 inclusions are mainly formed as deoxidization products [19], while MgO-Al_2O_3 inclusions are mainly generated by the combination of deoxidization products Al_2O_3 and [Mg] in liquid steel, which usually comes from lining or slag [20]. TiN and MnS inclusions are precipitates generated during steel solidification [21].

3.2. Fatigue test results

Figs. 5(a) and 5(b) show the specimens obtained before and after the fatigue tests. Fig. 6 shows the stress versus cycles (S–N) data of the fatigue tests. All of the cracks initiated in the broken specimens shown in Fig. 6 were caused by inclusions (i.e., Al_2O_3, MgO-Al_2O_3, and TiN).

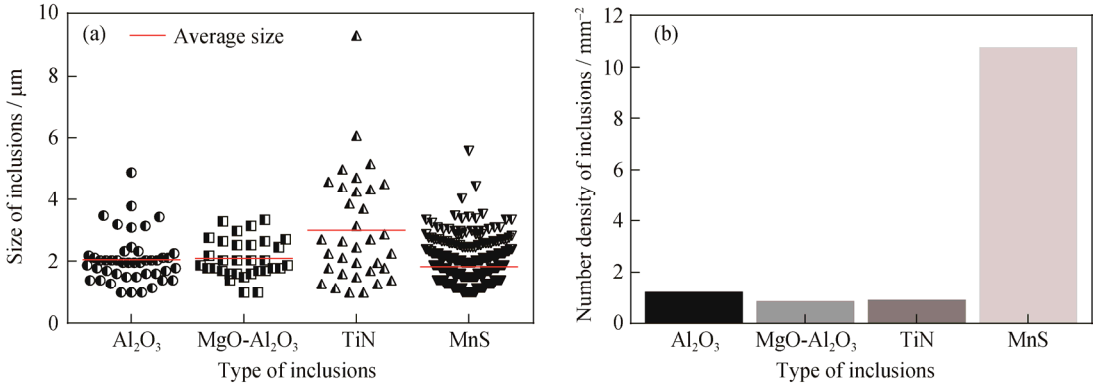

Fig. 4. Size (a) and number density (b) of the inclusions in GCr15 bearing steel.

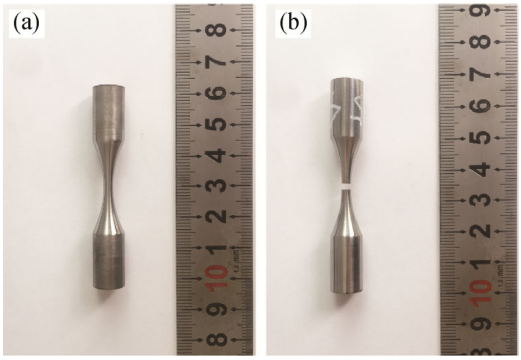

Fig. 5. Specimens obtained before (a) and after (b) the fatigue test.

Figs. 7 and 8 show the typical SEM images of the initiated cracks and the compositions of the inclusions. ODA structures were observed in both crack initiations in Figs. 7 and 8. In Fig. 7, gaps between MgO-Al_2O_3 inclusions and the steel matrix can be clearly observed in the crack initiation area. These inclusions remain unbroken, and the cracks originate from the gap between the steel matrix and this type of inclusions. Fig. 8 reveals no gap between TiN inclusions and the steel matrix at the point of crack initiation. Under this condition, the cracks originate from within the inclusions and propagate toward the steel matrix.

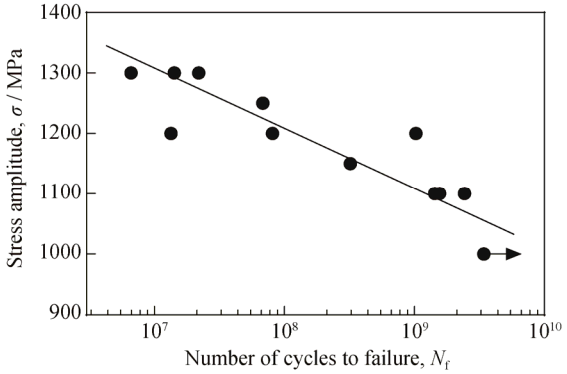

Fig. 6. S–N data of the internal crack initiation.

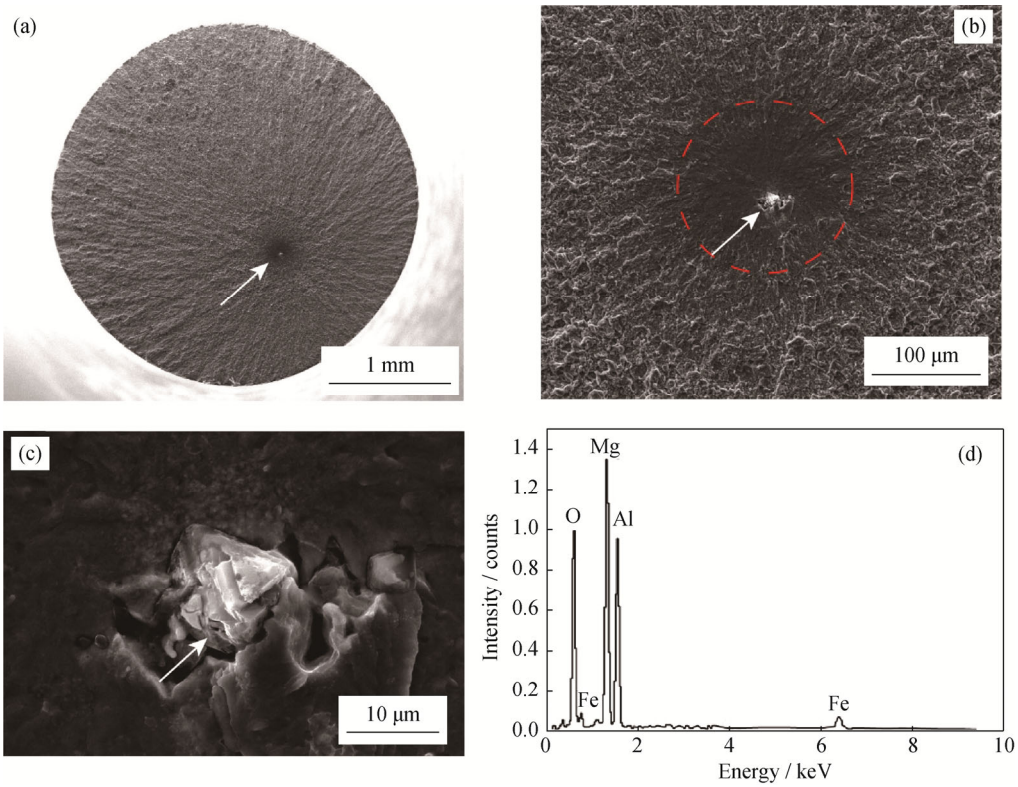

Fig. 7. Internal crack initiation at $MgO\text{-}Al_2O_3$ inclusions (σ = 1300 MPa, $N_f = 6.6 \times 10^6$ cycles): (a) fracture surface; (b) ODA structure; (c) an inclusion in crack initiation; (d) EDS analysis of the inclusion. Arrows indicate the same location of crack initiation.

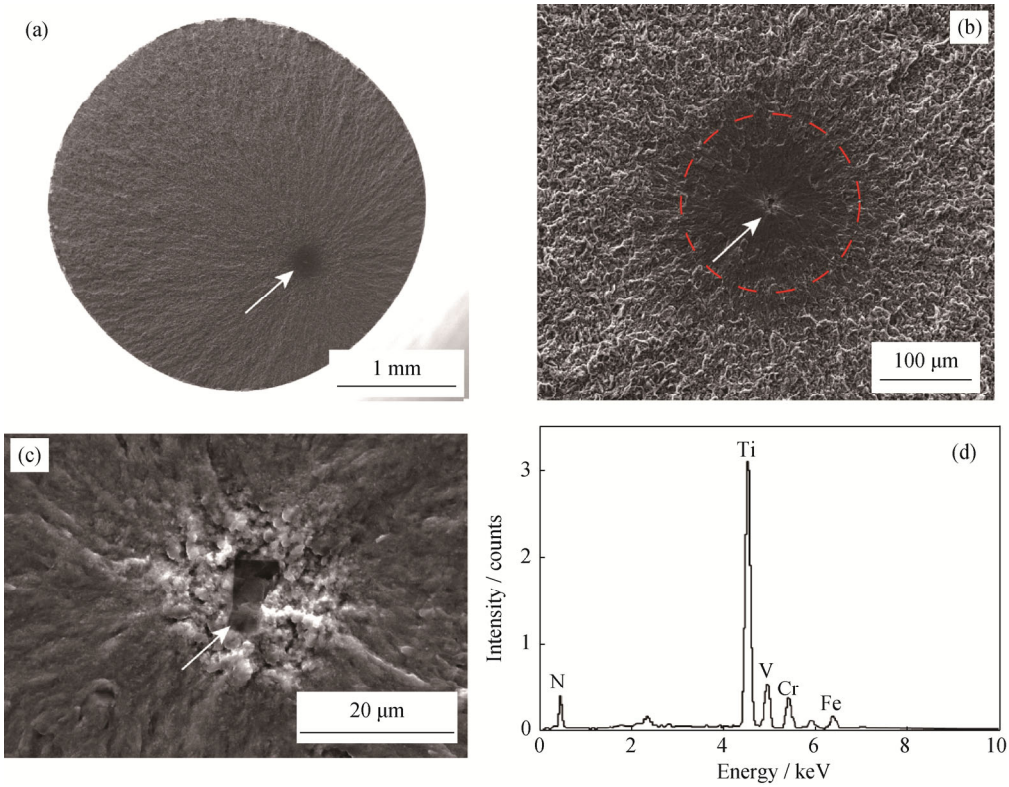

Fig. 8. Internal crack initiation at TiN inclusions (σ = 1150 MPa, $N_f = 3.2 \times 10^8$ cycles): (a) fracture surface; (b) ODA structure; (c) an inclusion in crack initiation; (d) EDS analysis of the inclusion. Arrows indicate the same location of crack initiation.

3.3. Effect of tessellated stresses of different inclusions on crack initiation

Based on Refs. [22–23], a model to calculate the tessellated stresses of inclusions was developed, as shown in Fig. 9. Assuming that the inclusion is spherical and that the radius of the matrix is far greater than the radius of the inclusion, the radial stress σ_R beneath the inclusion can be expressed by Eqs. (1) and (2):

$$\sigma_R = \frac{(\alpha_M - \alpha)\Delta T}{\frac{0.5(1+\upsilon_M)+(1-2\upsilon_M)d^3}{E_M(1-d^3)} + \frac{(1-2\upsilon)}{E}} \quad (1)$$

$$d = R / R_M \quad (2)$$

where α_M and α are the coefficients of linear expansion of the steel matrix and inclusion, respectively; v_M and v are the Poisson ratio's of the steel matrix and inclusion, respectively; E_M and E are the Young's moduli of the steel matrix and inclusion, respectively; ΔT is the difference between the holding temperature before vacuum quenching and the room temperature; R is the radius of the inclusion; and R_M is the radius of the steel matrix around a single inclusion, which can be calculated from the number density of inclusions, as shown in Fig. 4(a).

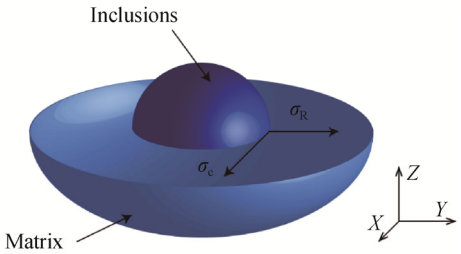

Fig. 9. Scheme of the model for tessellated stresses.

The σ_R at the interface between the steel matrix and main inclusions (i.e., Al_2O_3, MgO-Al_2O_3, MnS, and TiN) in Al-deoxidized bearing steel was calculated according to Eqs. (1) and (2), and the yield strength of the matrix was tested though tensile tests. The radius of inclusion R in the calculations was chosen to be the actual maximum inclusion size of GCr15 bearing steel in the present experiment, which is shown in Fig. 4(a). Table 2 shows the values of other parameters used for the calculations. Since the coefficient of thermal expansion of MnS is larger than that of the steel matrix, the resulting radial stress is a negative value. The calculated tessellated stresses of Al_2O_3, MgO-Al_2O_3, and TiN inclusions are shown in Fig. 10. The tessellated stresses of different types of inclusions varied, and the tessellated stresses of the four types of inclusions and the yield strength of steel matrix showed the following order: Al_2O_3 > MgO-Al_2O_3 > steel matrix > TiN > MnS.

Table 2. Mechanical parameters and coefficients of thermal expansion [22,24]

Material	Coefficient of linear expansion, α / (10^{-6}°C)	Young's modulus, E / GPa	Poisson's ratio, v
Al_2O_3	8.0	390	0.25
MgO-Al_2O_3	8.4	271	0.26
MnS	14.8	103	0.30
TiN	9.4	320	0.19
Matrix	23.0	210	0.50

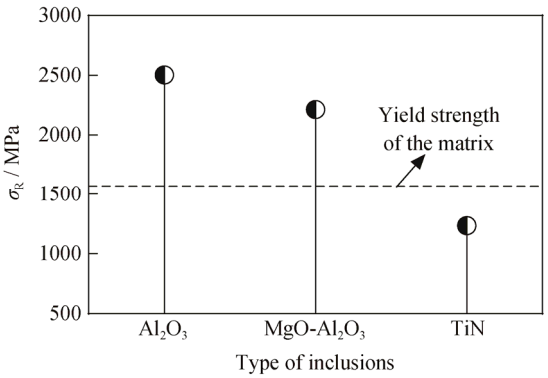

Fig. 10. Effect of inclusion types on tessellated stress.

When the tessellated stresses of the inclusions are larger than the yield strength of the steel matrix, these stresses will cause plastic deformation in the matrix around the inclusions, thereby generating gaps around the latter [19,23] that grow larger during the fatigue process. Thus, for fatigue damage caused by Al_2O_3 or MgO-Al_2O_3, obvious gaps can be observed between these inclusions and the steel matrix, consistent with the experimental results. As the gaps further develop, fewer interactions occur between the steel matrix and inclusions, and these types of inclusions can be regarded as holes when analyzing the fatigue process. However, when the tessellated stresses of inclusions are smaller than the yield strength of the steel matrix, no plastic deformation occurs in the steel matrix around these inclusions, leading to the formation of gaps only at their interface. Thus, for the fatigue damage caused by TiN or MnS, the inclusions are bonded to the steel matrix tightly and no obvious gaps are observed. Under this condition, these inclusions cannot be completely regarded as holes owing to the interaction between the matrix and inclusions.

3.4. Nano-mechanical characteristics of different inclusions and the steel matrix

Fig. 11 shows the load versus displacement curves of the steel matrix and inclusions (TiN and MnS) with tessellated stresses smaller than the yield strength of the matrix as determined from nanoindentation tests. The remnant indenta-

tion depth order is TiN > steel matrix > MnS; thus, the plastic deformation of MnS could be considered to be the smallest and the elastic resilience of MnS could be considered the best. In addition, the plastic deformation of TiN is the largest and the elastic resilience of TiN is the poorest. Therefore, when cracks are initiated due to inclusions with tessellated stresses smaller than the yield strength of the steel matrix (TiN and MnS), TiN will fracture before the steel matrix does while MnS will fracture only after the steel matrix does. Crack initiation caused by MnS was not observed in the present work.

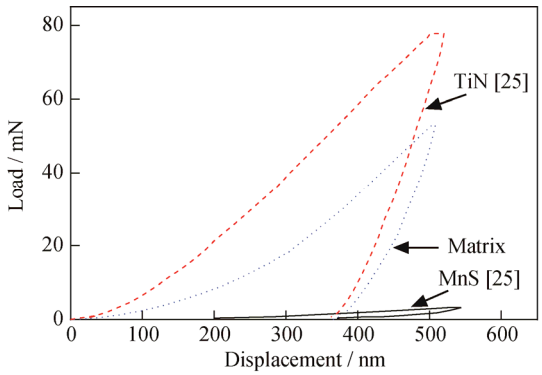

Fig. 11. Load versus displacement curves of the matrix and inclusions.

4. Conclusions

In summary, the effect of main inclusions on crack initiation in bearing steel in the VHCF regime was presented based on calculations of the tessellated stresses between these inclusions and a steel matrix. The tessellated stresses of inclusions in Al-deoxidized bearing steel and the yield strength of the steel matrix showed the order of Al_2O_3 > $MgO\text{-}Al_2O_3$ > steel matrix > TiN > MnS. Gaps formed around the inclusions with tessellated stresses larger than the yield strength of the matrix steel (i.e., Al_2O_3 and $MgO\text{-}Al_2O_3$) during the VHCF process. Under such conditions, cracks were first generated around gaps in the steel matrix. Other inclusions with tessellated stresses smaller than the yield strength of the steel matrix (i.e., TiN, MnS) were tightly bonded to the steel matrix during the VHCF process. As a result, cracks are initially generated within the inclusions. Considering the effect of inclusions on cracks, only the former type of inclusions could be regarded as holes.

Acknowledgements

This work was financially supported by the State Key Laboratory for Advanced Metallurgy Foundation (No. 41614014) and the National Natural Science Foundation of China (No. 51774031).

References

[1] H.Q. Nguyen, L. Gallimard, and C. Bathias , Numerical simulation of fish-eye fatigue crack growth in very high cycle fatigue, *Eng. Fract. Mech.*, 135(2015), p. 81.

[2] L.P. Xu, Q.Y. Wang, and M. Zhou, Micro-crack initiation and propagation in a high strength aluminum alloy during very high cycle fatigue, *Mater. Sci. Eng. A*, 715(2018), p. 404.

[3] Y.S. Hong, Z.Q. Lei, C.Q. Sun, and A.G. Zhao, Propensities of crack interior initiation and early growth for very-high-cycle fatigue of high strength steels, *Int. J. Fatigue*, 58(2014), p. 144.

[4] G.H. Gao, B.X. Zhang, C. Cheng, P. Zhao, H. Zhang, and B.Z. Bai, Very high cycle fatigue behaviors of bainite/martensite multiphase steel treated by quenching-partitioning-tempering process, *Int. J. Fatigue*, 92(2016), p. 203.

[5] Q.Y. Wang, J.Y. Berard, S. Rathery, and C. Bathias, Technical note high-cycle fatigue crack initiation and propagation behaviour of high-strength sprin steel wires, *Fatigue Fract. Eng. Mater. Struct.*, 22(1999), No. 8, p. 673.

[6] Y. Murakami, T. Nomoto, T. Ueda, and Y. Murakami, On the mechanism of fatigue failure in the superlong life regime ($N>10^7$ cycles). Part 1: influence of hydrogen trapped by inclusions, *Fatigue Fract. Eng. Mater. Struct.*, 23(2000), No. 11, p. 893.

[7] Y. Murakami, T. Nomoto, T. Ueda, and Y. Murakami, On the mechanism of fatigue failure in the superlong life regime ($N>10^7$ cycles). Part II: a fractographic investigation, *Fatigue Fract. Eng. Mater. Struct.*, 23(2000), No. 11, p. 903.

[8] Y. Murakami, T. Nomoto, and T. Ueda, Factors influencing the mechanism of superlong fatigue failure in steels, *Fatigue Fract. Eng. Mater. Struct.*, 22(1999), No. 7, p. 581.

[9] K. Shiozawa, Y. Morii, S. Nishino, and L. Lu, Subsurface crack initiation and propagation mechanism in high-strength steel in a very high cycle fatigue regime, *Int. J. Fatigue*, 28(2006), No. 11, p. 1521.

[10] K. Shiozawa, L. Lu, and S. Ishihara, *S–N* curve characteristics and subsurface crack initiation behaviour in ultra-long life fatigue of a high carbon-chromium bearing steel, *Fatigue Fract. Eng. Mater. Struct.*, 24(2001), No. 12, p. 781.

[11] T. Sakai, Y. Sato, and N. Oguma, Characteristic S–N properties of high-carbon–chromiumbearing steel under axial loading in long-life fatigue, *Fatigue Fract. Eng. Mater. Struct.*, 25(2002), No, 8-9, p. 765.

[12] Y. Murakami and M. Endo, Effects of defects, inclusions and inhomogeneities on fatigue strength, *Int. J. Fatigue*, 16(1994), No. 3, p. 163.

[13] Y. Murakami, S. Kodama, and S. Konuma, Quantitative

evaluation of effects of nonmetallic inclusions on fatigue strength of high strength steel, *Trans. Jpn. Soc. Mech. Eng. A*, 500(1988), No. 54, p. 688.

[14] Y. Murakami and H. Usuki, Prediction of fatigue strength of high-strength steels based on statistical evaluation of inclusion size, *Trans. Jpn. Soc. Mech. Eng. A*, 510(1989), No. 55, p. 213.

[15] C. Sun, J. Xie, A. Zhao, Z. Lei, and Y. Hong, A cumulative damage model for fatigue life estimation of high-strength steels in high-cycle and very-high-cycle fatigue regimes, *Fatigue Fract. Eng. Mater. Struct.*, 35(2012), No. 7, p. 638.

[16] W. Li, T. Sakai, and H. Deng, Statistical evaluation of very high cycle fatigue property of high carbon chromium bearing steel under axial loading, *Mater. Sci. Technol.*, 32(2016), No. 11, p. 1094.

[17] D. Spriestersbach, P. Grad, and E. Kerscher, Influence of different non-metallic inclusion types on the crack initiation in high-strength steels in the VHCF regime, *Int. J. Fatigue*, 64(2014), p. 114.

[18] U. Karr, R. Schuller, M. Fitzka, B. Schönbauer, D. Tran, B. Pennings, and H. Mayer, Influence of inclusion type on the very high cycle fatigue properties of 18Ni maraging steel, *J. Mater. Sci.*, 52(2017), No. 10, p. 5954.

[19] Z.Y. Deng and M.Y. Zhu, Evolution mechanism of non-metallic inclusions in Al-killed alloyed steel during secondary refining process, *ISIJ Int.*, 53(2013), No. 3, p. 450.

[20] H. Itoh, M. Hino, and S. Banya, Thermodynamics on the formation of non-metallic inclusion of spinel ($MgO{\cdot}Al_2O_3$) in liquid steel, *Tetsu-to-Hagane*, 84(1998), No. 2, p. 85.

[21] C. Gu, Y.P. Bao, and L. Lin, Cleanliness distribution of high-carbon chromium bearing steel billets and growth behavior of inclusions during solidification, *Rev. Metal.*, 53(2017), No. 1, p. 1.

[22] D. Brooksbank and K.W. Andrews, Tessellated stresses associated with some inclusions in steel, *J. Iron Steel Inst.*, 207(1969), No. 4, p. 474.

[23] Y. Ma, T. Pan, B. Jiang, Y.H. H. Su, and Y. Peng, Study of the effect of sulfur contents on fracture toughness of railway wheel steels for high speed train, *Acta Metall. Sin.*, 47(2011), No. 8, p. 978.

[24] D. Brooksbank and K.W. Andrews, Thermal expansion of some inclusions found in steels and relation to tessellated stresses, *J. Iron Steel Inst.*, 206(1969), No. 6, p. 595.

[25] Y.N. Wang, Y.P. Bao, and M. Wang, Nanoindentation characterization of non-metallic inclusions in free cutting steel, *J. Univ. Sci. Technol. Beijing*, 36(2014), No. 7, p. 903.